Anatomy and activity patterns in a multifunctional motor neuron and its surrounding circuits

Short title: *Imaging and connectome of leech ganglion*

One-sentence summary: *Voltage-dye imaging followed by serial blockface electron microscopy of the same ganglion reveals structure–function relationships of leech motor behaviors.*

Mária Ashaber[1*], Yusuke Tomina[1,2*], Pegah Kassraian-Fard[1*], Eric A. Bushong[3], William B. Kristan Jr[3], Mark H. Ellisman[4,5] and Daniel A. Wagenaar[1+]

1 Division of Biology and Biological Engineering, California Institute of Technology, Pasadena, CA, USA.

2 Faculty of Science and Technology, Keio University, Yokohama, Kanagawa, JAPAN.

3 Division of Biological Sciences, University of California, San Diego, La Jolla, CA, USA.

4 National Center for Microscopy and Imaging Research, University of California, San Diego, La Jolla, CA, USA.

5 Department of Neurosciences, UCSD School of Medicine

* These authors contributed equally.

\+ Correspondence: Caltech 139-74, Pasadena, CA 91125, USA; daw@caltech.edu; ++1-626-395-8567.

Graphical abstract

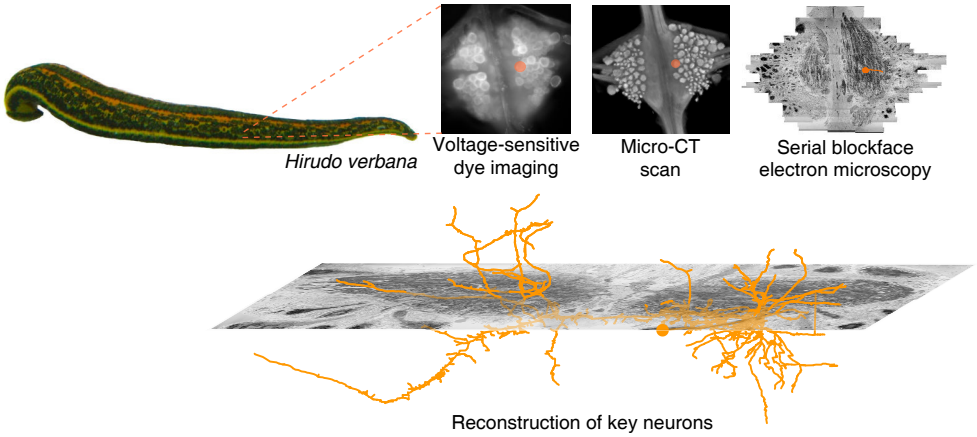

Approach. Several fictive behaviors were induced in the isolated nervous system of a medicinal leech while one segmental ganglion was imaged using a voltage-sensitive dye. After fixation and resin embedding, the ganglion was x-ray-imaged to verify that the geometry of somata was preserved. Finally, the neuropil was imaged at nanometer resolution with serial blockface electron microscopy and selected neurons were manually traced.

Abstract

Dorsal Excitor motor neuron DE-3 in the medicinal leech plays three very different dynamical roles in three different behaviors. In swimming, it oscillates at a relatively rapid 2 Hz in antiphase to its Ventral Excitor counterpart (VE-4) and controls the local dorsal flexion phase of the swim rhythm. In crawling, it is active in phase with VE-4 and controls the contraction phase of the crawl rhythm. In "local bending" it operates in tight concert with its contralateral homolog as well as VE-4 to precisely deform the local body wall away from a mechanical stimulus. Without rewiring its anatomical connectivity, how can a motor neuron dynamically switch roles to play its appropriate role in various behaviors? We used voltage-sensitive dye imaging to record from DE-3 and most other neurons in the segmental ganglion of the leech during fictive versions of the three behaviors. Then we re-imaged the same ganglion using serial blockface electron microscopy and traced all of DE-3's processes. Further, we traced back the processes of all of DE-3's presynaptic partners to their respective somata. This allowed us to analyze the relationship between circuit anatomy and the activity patterns it sustains. We found that input synapses important for all of the behaviors were widely distributed over DE-3's branches, yet that functional clusters were different during (fictive) swimming vs. crawling.

Introduction

Some neural circuits are responsible for only one specialized function. Examples include the exquisitely tuned delay lines that barn owls use to locate sounds (Carr and Konishi, 1988) and the motor neurons that control the honeybee's stinger (Ogawa et al., 1995). In the early days of neuroscience, those circuits received most attention, likely because they are in important ways more tractable. In most animals' central nervous systems, however, many circuits respond to stimuli of multiple sensory modalities or control more than one behavior (Briggman and Kristan, 2008). Increasingly, even sensory brain areas once considered unimodal are found to be modulated by or to directly respond to other sensory modalities, or to be modulated by behavioral state. For instance, auditory stimuli can modulate activity in the human visual cortex (Plass et al., 2019) (and not just in blind subjects (Bedny et al., 2015)). Likewise, motor cortex activity can be modulated not just by visual presentation of images of relevant body parts, but even in a working memory task in the absence of immediate stimuli (Galvez-Pol et al., 2018). All of these forms of multifunctionality likely contribute to the versatility of large brains like ours and may help smaller animals use their more constrained neural hardware more efficiently (Briggman and Kristan, 2008).

A particularly interesting situation occurs when multifunctional circuits converge onto a single motor neuron which plays distinct roles in different behaviors (Miroschnikow et al., 2018; Zarin et al., 2019). What functional and anatomical aspects of the converging pathways permit the output neuron to play its various roles? Control of locomotion in the medicinal leech (*Hirudo verbana*)

is a prime example of a system organized in this manner. In each of the animal's segmental ganglia, partially overlapping circuits generate the rhythms for swimming and crawling as well as the dynamics of an escape behavior known as the local bend (Kristan et al., 2005; Briggman et al., 2005; Tomina and Wagenaar, 2017). These circuits have a common output in a motor neuron called DE-3 that excites the animal's dorsal longitudinal muscles.

To study the mechanisms underlying the versatility of multifunctional circuits, one would ideally like to record from every single neuron in a nervous system during all of the behaviors the animal can execute, and then reconstruct the anatomical connections between those neurons. Once a mere dream, this is rapidly becoming practicable: Activity imaging using calcium dyes has advanced to the point where simultaneous recordings from the vast majority of individual neurons in smaller species can be accomplished, for instance in larval zebrafish (Ahrens et al., 2013). This technique has even been applied to behaving animals (Jiao et al., 2018). Likewise, anatomical imaging using electron microscopy has advanced to the point that brains as large as that of the fruit fly *Drosophila melanogaster* can be imaged—and substantial fractions of their circuitry reconstructed—at a synaptic resolution (Zheng et al., 2018; Bates et al., 2020; Xu et al., 2020; Maniates-Selvin et al., 2020). Even small vertebrate brains like that of larval zebrafish are yielding to this approach (Hildebrand et al., 2017).

To bring form and function together, an anatomical atlas based on electron microscopy can be combined with functional studies that use the split-GAL4 system to target indivual neurons and identify them with neurons in the anatomical map (Eichler et al., 2017; Eschbach et al., 2020). This is an immensely powerful approach because a single (costly and time consuming) EM run can be used with an unlimited number of functional studies. However, cross-identification of neurons between EM and functional imaging in this approach is ultimately limited by the fact that all nervous systems, even the simplest ones, exhibit considerable variability in their connectomes (Bhattacharya et al., 2019). Accordingly, robustly linking function to connectivity requires a combined anatomical and functional assessment within the same animal (Bargmann and Marder, 2013). Nearly a decade ago, back-to-back papers in *Nature* described two-photon calcium imaging in the mouse visual cortex followed by serial transmission electron microscopy of a small volume of that same cortex (Bock et al., 2011) and two-photon calcium imaging in the mouse retina followed by serial block face electron microscopy of that same retina (Briggman et al., 2011). This approach, "Correlated Light and Electron Microscopy" or CLEM (de Boer et al., 2015), has since allowed the quantification of synaptic connections between functionally identified neurons that control eye movement in the larval zebrafish (Vishwanathan et al., 2017), a reconstuction of the connections in the olfactory bulb of another larval zebrafish in which neural responses to eight different odors had been recorded prior to sectioning (Wanner and Friedrich, 2020), and a critical re-assessment of the mechanisms of selectivity to particular sensory features in neurons of the mammalian visual cortex (Scholl et al., 2019).

For the present study of multifunctional behavioral circuits, we chose to use a voltage-sensitive dye (VSD) (Grinvald and Hildesheim, 2004; Kulkarni and Miller, 2017) rather than a calcium dye

because it can capture faster temporal dynamics, potentially even recording individual action potentials, as well as both excitatory and inhibitory synaptic potentials. We used a fast, high-sensitivity VSD (Woodford et al., 2015) to record the neuronal activity in a segmental ganglion of the medicinal leech *Hirudo verbana* while its nervous system expressed several (fictive) behaviors. Then, to map the circuits underlying those behaviors with synapse-level resolution, we re-imaged the same individual ganglion using serial blockface electron microscopy (SBEM) (Lippens et al., 2019). Finally, we traced the full arborization of the DE-3 motor neuron and the relevant parts of all its presynaptic partners, to enable comparison between functional and anatomical features of the circuit. The "Graphical Abstract" illustrates the overall approach. To our knowledge, this is the first time VSDs and SBEM have been combined at this scale.

Results

Voltage-dye imaging of behavior

The nervous system of the leech comprises cephalic ganglia, a tail ganglion, and 21 nearly identical segmental ganglia connected by a ventral nerve cord (Muller et al., 1981; Wagenaar, 2015). Each ganglion consists of about 400 neurons (Macagno, 1980) with cell bodies arranged in a spherical monolayer around a central neuropil. In the neuropil, neurons communicate through chemical and electrical synapses located along extensively branched neurites (Muller and McMahan, 1976; Fan et al., 2005; Pipkin et al., 2016). The leech is an ideal model organism for this type of work, because it robustly expresses several behaviors even in reduced preparations (Kristan et al., 2005), its neurons are uncommonly accessible to physiological recording, and its cell bodies are relatively large and thus yield strong VSD signals (Briggman et al., 2005). Crucially, an individual segmental ganglion is a good stand-in for a whole nervous system, because its neurons capture the entire pathway from sensory input through self-generated interneuronal rhythms to motor output (Kristan et al., 2005), which is why we focused our imaging efforts there.

We expressed (fictive) swimming, crawling, and local bending behavior in the isolated nervous system of a single leech following the same protocol used for a previous extensive study of these behaviors using VSD imaging in a larger group of animals (Tomina and Wagenaar, 2017). As in the previous study, one segmental ganglion in the chain was prepared for VSD imaging and we recorded from both the ventral and dorsal aspects simultaneously with a double-sided fluorescence microscope (Fig. 1a). We were able to record from 250 neurons simultaneously, similar to our previous results. Fictive swimming was induced by electrical stimulation of a posterior segment, which resulted in characteristic rhythmic activity in dorsal motor neurons and many other neurons on both sides of the ganglion (Fig. 1b). Coherence analysis confirmed that the rhythms of the various neurons were indeed related to the fictive behavior (Fig. 1c, d). In a similar manner, we induced fictive crawling (Fig. 2) and local bending (Fig. 3).

We established a mapping between the neurons seen in the VSD images and the canonical

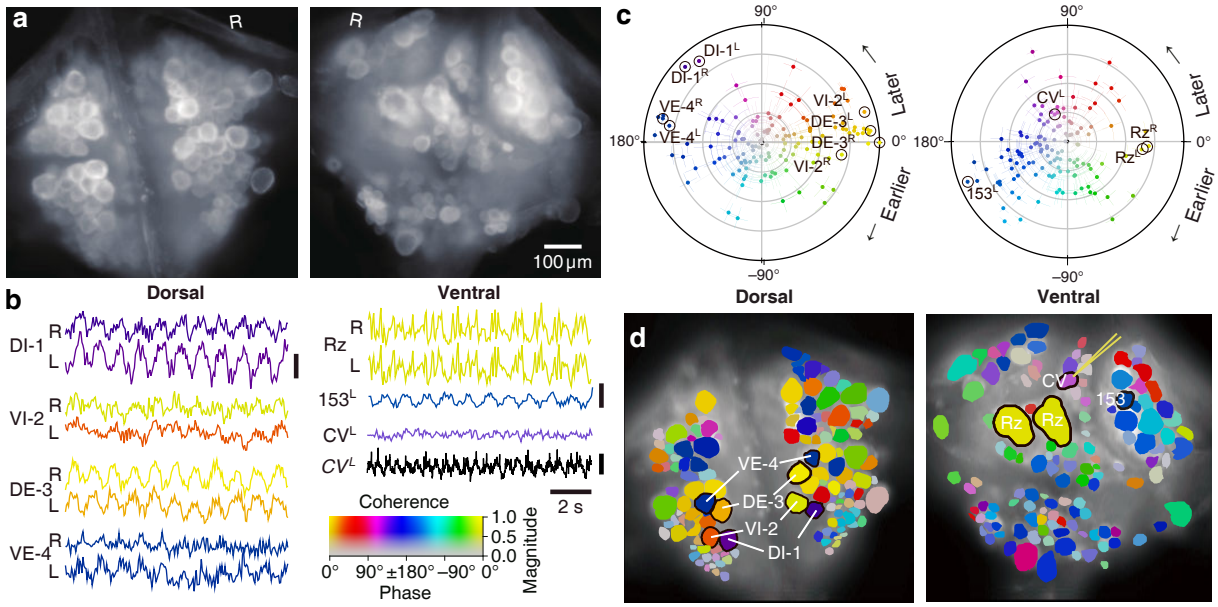

Figure 1: Fictive swimming imaged using VSD. **a**. Images of the dorsal (*left*) and ventral (*right*) aspects of a leech ganglion simultaneously obtained using a double-sided microscope. "R" indicates the right side of the ganglion (i.e., the animal's right when dorsal side up). **b**. Selected VSD traces during fictive swimming. From the dorsal surface: dorsal and ventral inhibitory and excitatory motor neurons DI-1, VI-2, DE-3, and VE-4; from the ventral surface: the Retzius cells (neuromodulatory interneurons) and cell 153^{L} (an interneuron). All of those cells are known to be rhythmically active during swimming. Also shown is CV^{L}, an excitor of ventrolateral circular muscles that was intracellularly recorded during the trial as a control to verify that fluorescence signals reflect membrane potential changes as they should. Scale bars: 0.2% relative fluorescence change, 5 mV membrane potential change. **c**. Magnitude (radial axis from 0 to 1) and phase (angular coordinate) of the coherence of activity in individual neurons with the swim rhythm in motor neuron DE-3^{R}. Error bars indicate confidence intervals based on a multi-taper estimate. dorsal (*left*) and ventral (*right*) surfaces of the ganglion. Colors of cell bodies indicate coherence relative to DE-3^{R}. The yellow needle on CV^{L} indicates a sharp electrode for intracellular recording. Color scale applies to all panels.

maps of the ganglion (Wagenaar, 2017) based on geometry and on the involvement of the neurons in the various behaviors.

X-ray tomography connects functional and anatomical image stacks

At the end of the (fictive) behavior experiment, the ganglion was fixated and embedded in a resin. To correlate light and electron microscopy, we then re-imaged the ganglion using x-ray tomography (Bushong et al., 2015) and verified that the cell bodies seen in the VSD images could still be identified (Fig. 4a). The x-ray image stack was also used to trace neuronal processes from the somata to the edge of the neuropil (Fig. 4b). This obviated the need to capture the somata in the subsequent electron microscopy, and instead allowed us to restrict the EM effort largely to the neuropil.

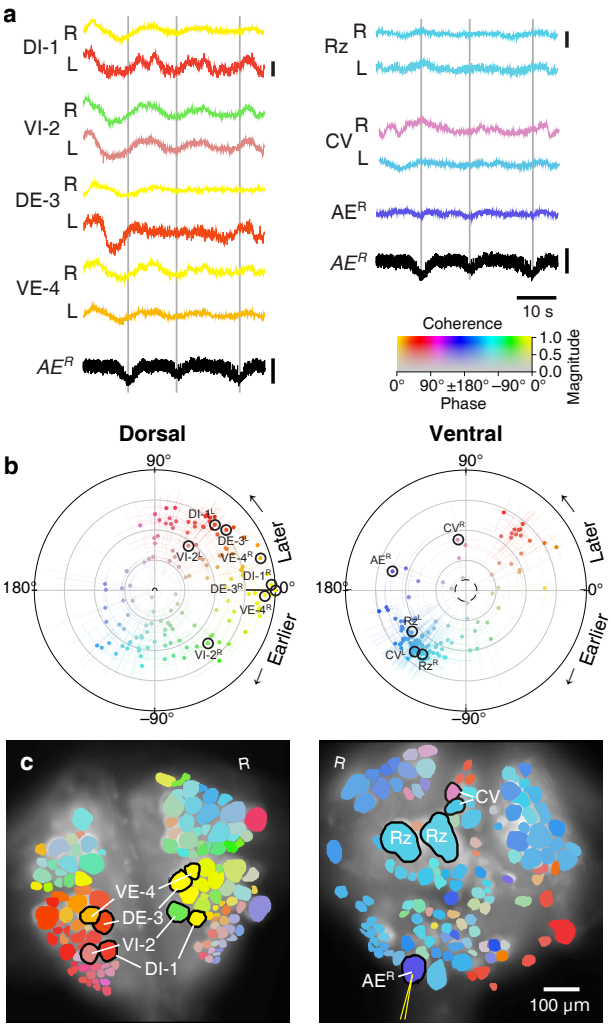

Figure 2: Fictive crawling imaged using VSD. **a**. Selected VSD traces during fictive crawling. From the dorsal surface: dorsal and ventral inhibitory and excitatory motor neurons DI-1, VI-2, DE-3, and VE-4; from the ventral surface: the Retzius cells and CV cells. All of those cells are known to be rhythmically active during crawling. Below the VSD traces, a simultaneously recorded intracellular trace of the annulus erector motor neuron AE^R is displayed (in both columns). Scale bars: 0.2%, 10 mV. Gray lines mark hyperpolarized phase of AE^R. **b**. Magnitude and phase of the coherence of activity in individual neurons with the crawl rhythm in motor neuron DE-3^R. **c**. Coherence maps of the VSD signals of all cells on the dorsal (*left*) and ventral (*right*) surfaces of the ganglion. Colors of cell bodies indicate coherence relative to DE-3^R. The yellow needle on AE^R indicates a sharp electrode for intracellular recording. Color scale applies to all panels.

Electron microscopy

We chose serial blockface electron microscopy (SBEM) over serial-section transmission EM (Harris et al., 2006) because SBEM can reliably process large numbers of slices with much lower risk of sectioning artifacts. We acquired 78,803 images from 9604 slices, totaling 22.8 terapixels. We periodically paused the acquisition to adjust the imaging area so as to include the entirety of the neuropil but not too much additional space.

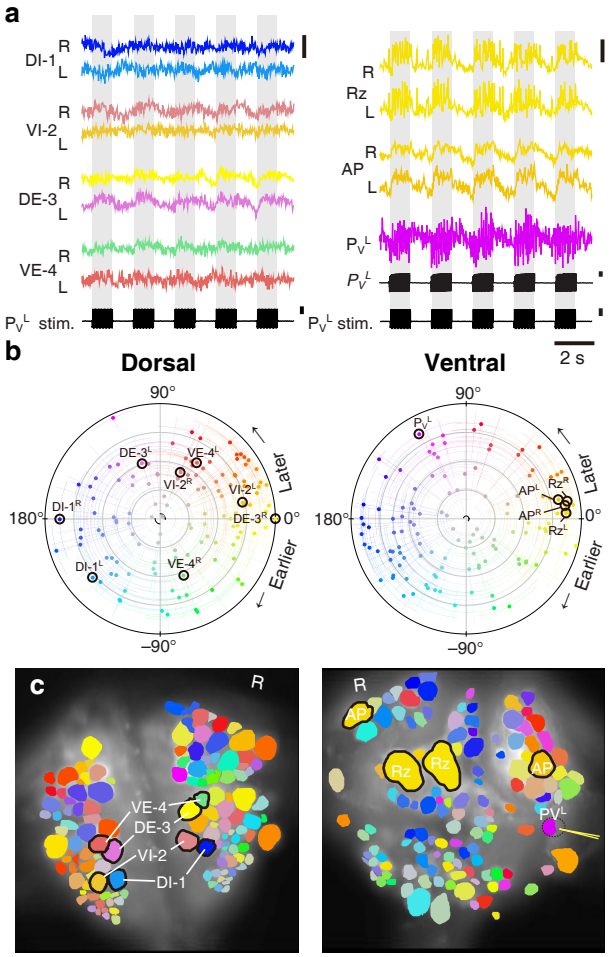

Figure 3: Fictive local bending imaged using VSD. **a**. Selected VSD traces during fictive local bending. From the dorsal surface: dorsal and ventral inhibitory and excitatory motor neurons DI-1, VI-2, DE-3, and VE-4; from the ventral surface: the Retzius cells, "Anterior Pagoda" cells ("AP"; well-known postsynaptic partners of the P cells with unknown function). Below the traces, a simultaneously recorded intracellular trace of the P_V^L cell is displayed with injected current trains (in both columns). Scale bars: 0.2% relative fluorescence change, 100 mV membrane potential change, 2 nA injected current. **b**. Magnitude and phase of the coherence of activity in individual neurons with the local bend rhythm in DE-3^R. **c**. Coherence maps of the VSD signals of all cells on the dorsal (*left*) and ventral (*right*) surfaces of the ganglion. Colors of cell bodies indicate coherence relative to DE-3^R. A yellow needle on P_V^L indicates a sharp electrode for electrical stimulation. Note that P_V^L was only weakly stained by the VSD because it was left partially covered with sheath tissue to preserve its health.

Tracing a motor neuron and all its synaptic inputs

We manually traced motor neuron DE-3^R, a key motor neuron for all of the behaviors included in our functional data set. The combined path length of the entire arborization of DE-3^R was 6,109 μm (Fig. 5a, b; Fig. 6a). In addition to tracing the neuron, we marked all of its input synapses and then traced each of its presynaptic partners to their somata. Several visually distinct types of synapses were found, among which most prominently: (1) bright terminals with large dark vesicles (Fig. 5c)

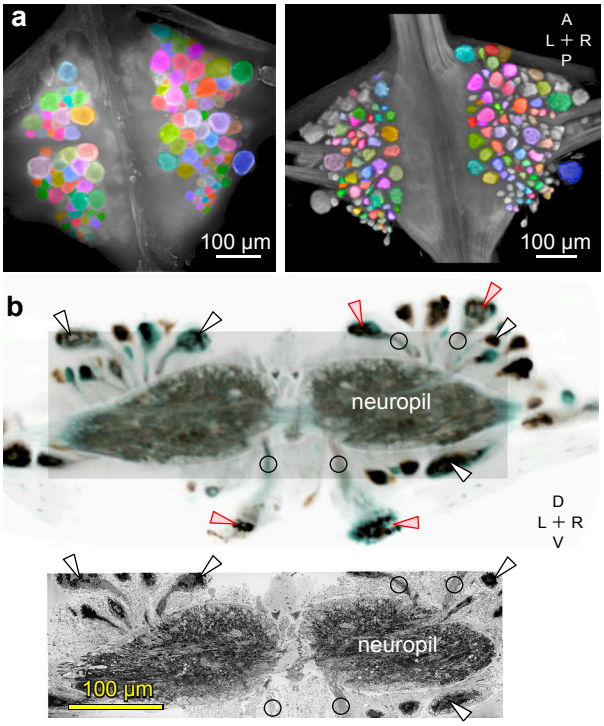

Figure 4: Mapping between functional and anatomical images. **a**. Light micrograph (*left*) and x-ray image (*right*) of the ganglion in which we recorded neuronal activity using a VSD. Matching colors label the same cells on the two images. A: Anterior, P: Posterior, L: Left, R: Right. **b**. Transverse section from X-ray tomographic image stack of the ganglion (*top*). Only the shaded area was imaged with SBEM (*bottom*). Arrowheads mark several somata that are (*white*) or are not (*red*) included in the SBEM volume. Circles mark neurites that facilitated complete mapping between the two imaging modalities. D: Dorsal, V: Ventral. Note that the x-ray image in (b) is shown in reverse video relative to the x-ray image in (a) for easier visual comparison with the SBEM image.

and (2) darker terminals with smaller vesicles that occurred mainly in fiber endings and varicosities (Fig. 5d). The small vesicles are barely resolved in our data set and appear merely as fields of granules. We used TEM on thin slices of a second ganglion to confirm our interpretation of these granules as vesicles (Fig. S1). No attempt has been made as of yet to interpret the anatomically distinct types of synapses as physiological classes.

We identified 531 synapses onto DE-3^{R}. Of these, 44 were formed by cells with somata in neighboring ganglia that were not included in our EM volume. Of the rest, 387 could be traced to their somata with a high degree of confidence. To avoid false positives, we only considered presynaptic neurons that formed at least two synapses onto DE-3^{R}. There were 51 of those. Of those, 35 could be confidently matched to cell bodies seen in the VSD record, and of those, 10 could be confidently matched to specific identified neurons on the canonical map with previously described functions (Fig. 6b, 7a, and Table 1). For the others, we assigned previously unused cell numbers from the canonical map (Wagenaar, 2017) based on soma location and size Fig. 6c. (If there were no unused cell numbers in the vicinity, we re-used a previously used cell number but

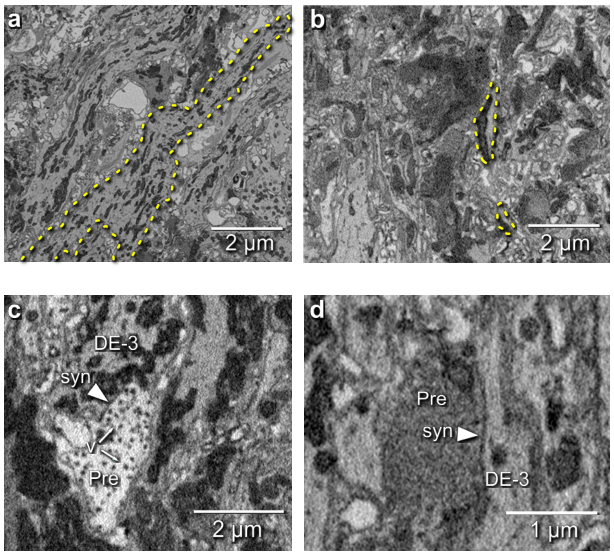

Figure 5: Electron microscopic tracing: neurites and synapses of motor neuron DE-3^{R}. **a**. The principal neurite of DE-3^{R} near its entrance to the neuropil (*dashed yellow outline*). **b**. Two branches of the neurite of DE-3^{R} (*dashed outlines*). **c**. A synaptic connection onto DE-3^{R} from an inhibitory motor neuron (DI-1^{R}). *Arrowheads*: synapses, *Pre*: presynaptic terminal, *v*: vesicles. **d**. A synapse onto DE-3^{R} from an interneuron (cell 24 on the canonical map (Wagenaar, 2017)).

Table 1: Identified partner neurons of DE-3^{R}.
These synaptic partners could be confidently assigned as previously described neurons.

Cell	Synapse count	Known function
DI-1^{L}	4	Inhibitor of dorsomedial longitudinal muscles
DI-1^{R}	52	Inhibitor of dorsomedial longitudinal muscles
8^{R}	13	Excitor of ventral longitudinal muscles
101^{R}	2	Inhibitor of dorsoventral muscles
102^{R}	6	Inhibitor of dorsal longitudinal muscles
107^{R}	12	Excitor of dorsomedial longitudinal muscles
109^{R}	7	Excitor of lateral dorsoventral muscles
117^{R}	16	Excitor of medial dorsoventral muscles
L^{R}	3	Excitor of dorsal and ventral longitudinal muscles

placed a question mark in the figure to indicate that we do not know if our cell and the previously described cell are the same.) The figure also shows some of the cells that we could not confidently link to the VSD record. We did not assign preliminary numbers to those.

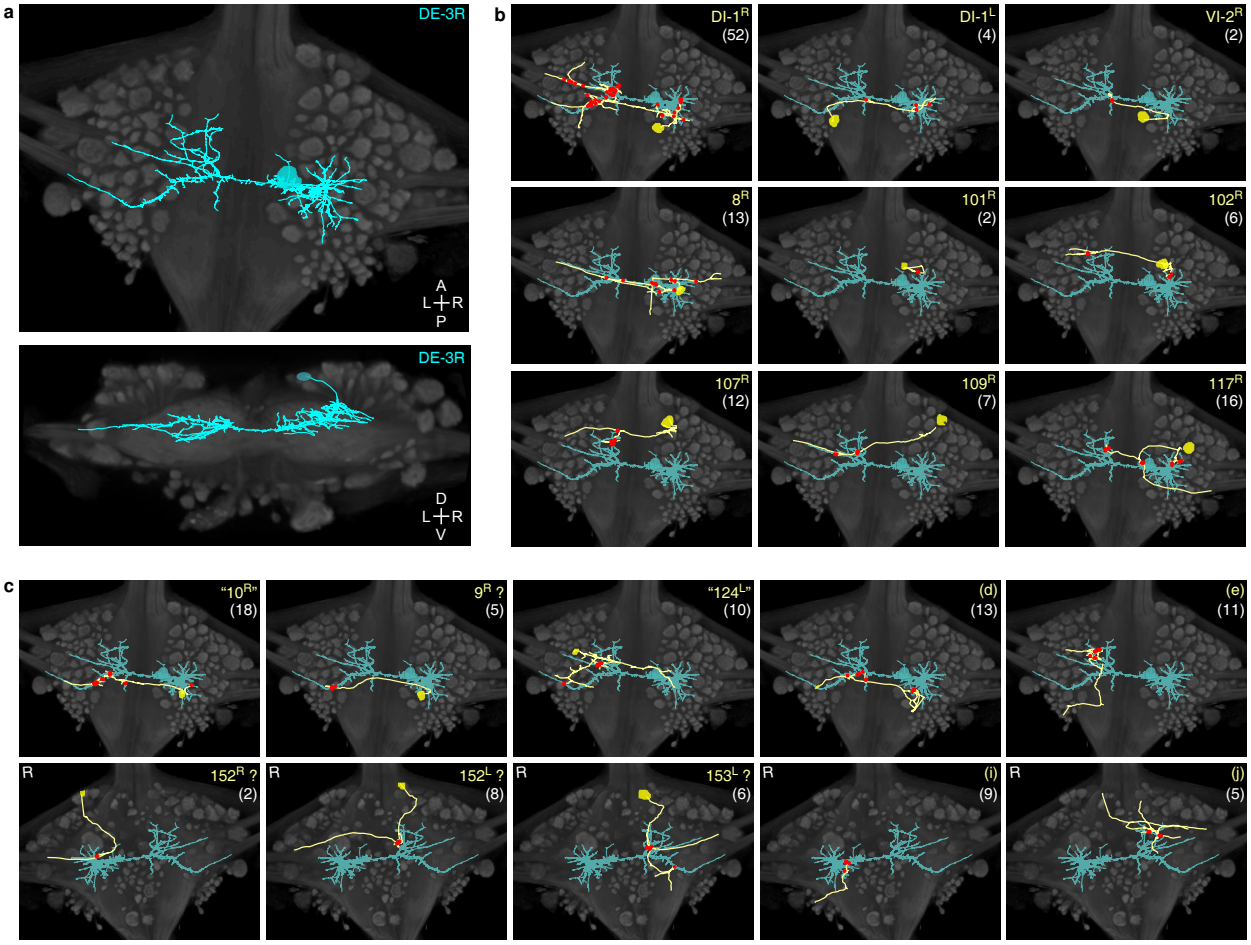

Figure 6: Traced neuronal arborizations **a**. Fully reconstructed arborization of DE-3^{R} overlaid on a dorsal projection and a transverse section of the micro-CT data. **b**. A selection of presynaptic partners with previously known identities. **c** A selection of presynaptic partners not matched to neurons previously described in the literature. (Top row: cell bodies on dorsal aspect; bottom row: cell bodies on ventral aspect of the ganglion.) Other cells in this category are 20^{R}, 25^{R}, 154^{R}, 156^{L}. Numbers in parentheses are number of synapses between each cell and DE-3^{R}.

Linking form to function

The availability of both functional (VSD) and anatomical (SBEM) information from the same individual ganglion allowed us to ask questions that relate form to function. As a first example, we asked whether synapses with different valences (excitatory or inhibitory) were differently distributed along the arbors of DE-3^{R}. Excitation and inhibition rely on different physiological processes and have asymmetric effects on cell membrane potential. Accordingly, one might expect that excitatory and inhibitory cells synapse onto their target cells in distinct spatial patterns. For instance, to achieve shunting inhibition, inhibitory synapses would have to be located close to the target cell's spike initiation zone. We therefore considered all the input synapses onto DE-3^{R} from neurons with previous descriptions in the literature, and annotated them as either excita-

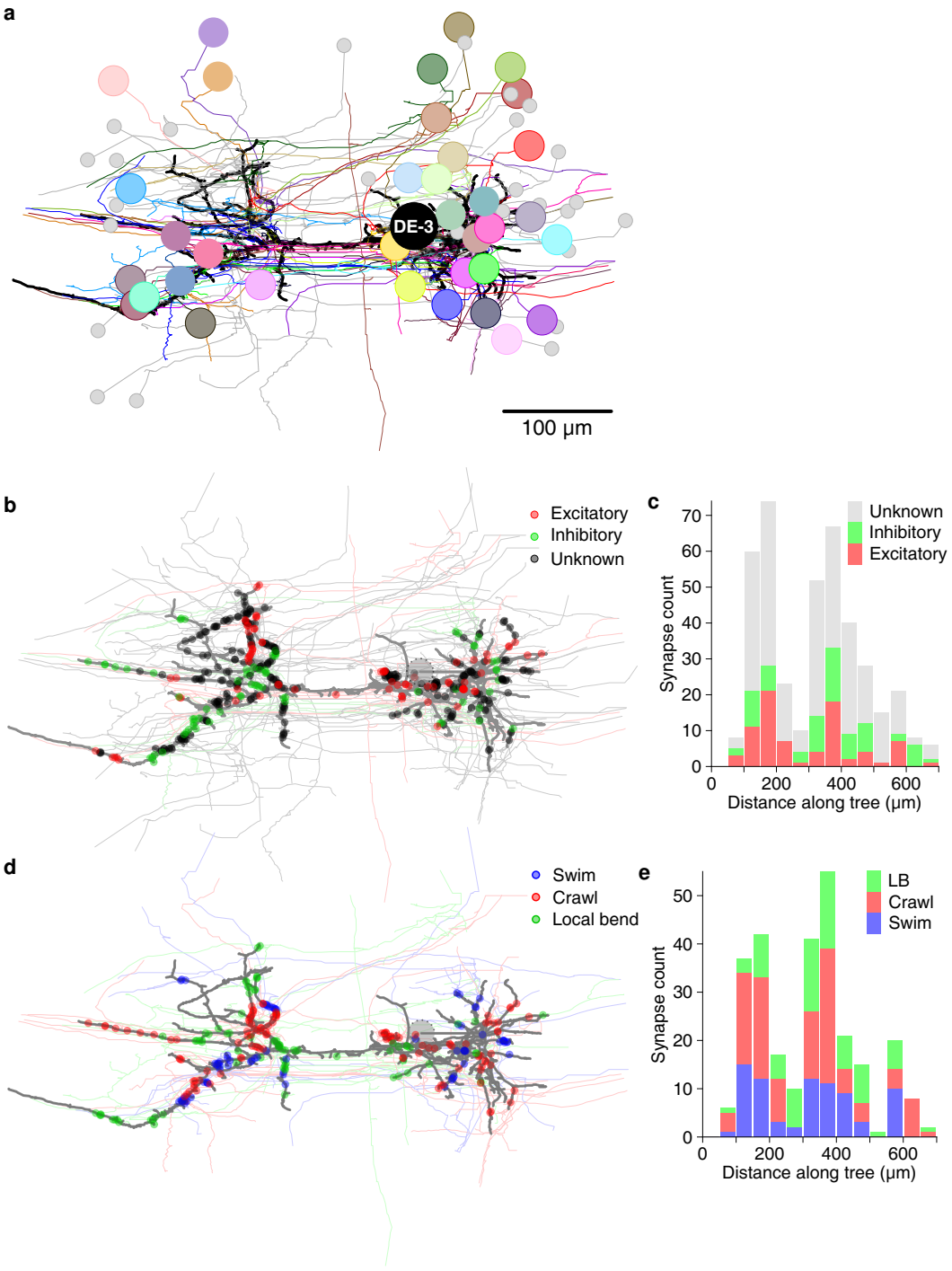

Figure 7: Partner neurons of DE-3^{R} with multiple synapses. **a**. Full tracing of DE-3^{R} (thick black line, soma location marked "DE-3") and backtracings of all synaptic partners. Partners that we could identify with cells in the VSD recording are marked with (arbitrary) colors. Small gray disks indicate partner neurons that could not be cross-identified between EM and VSD image stacks. See also Supplementary Movie 1. **b**. Spatial distribution of excitatory and inhibitory synapses onto DE-3^{R}. **c**. Histogram of the length of the paths between those synapses and the soma. **d**. Spatial distribution of synapses more strongly associated with a certain behavior. **e**. Histogram of the length of the paths between those synapses and the soma. (LB: Local bend).

tory or inhibitory (Fig. 7b). We did not however find any obvious differences between the spatial distributions of excitatory and inhibitory synapses (Fig. 7c).

For a second example, we started from the premise that motor neuron DE-3^{R}, as an output neuron of a multifunctional circuit, must integrate a diverse set of inputs in a flexible manner to accurately generate distinct behaviors. This versatility requires a dynamic functional reorganization of the underlying structural circuit. The question hence arises what the principles governing this dynamic reorganization are. We considered whether the anatomy of DE-3^{R} facilitates reading out the different patterns of synchronicity in its presynaptic partners during different behaviors.

We first looked at all neurons that we could cross-reference between EM and VSD recordings (regardless of whether the function of those neurons had previously been described) and, for each of the three behaviors, selected the cells that exhibited the highest coherence with DE-3^{R} in that behavior (see Methods). We asked whether cells associated in that way with a specific behavior would form synapses in specific locations, but found that that was not the case at the macroscopic scale (Fig. 7d, e).

The absence of an obvious modular organization of DE-3^{R} at the macroscopic level leaves open the possibility of structure at the micrometer scale exists that relates to the different behaviors. To test that idea, we asked whether synchronously active presynaptic partners form synapses onto DE-3^{R} that are spatially clustered. Such spatial clustering of synapses of synchronized cell assemblies has been previously observed in other model organisms (Takahashi et al., 2012; Varga et al., 2011).

Our spatial clustering algorithm had two free parameters: the maximum allowable distance between nearest neighbor synapses (d_{NN}), and the maximum overall cluster extent (d_{ext}); see inset to Fig. 8b and Methods. We searched through all biologically plausible combinations of values for these parameters. At all points in this parameter space, the algorithm identified a multitude of synaptic clusters on the neurites of DE-3^{R}. Most of these clusters contained synapses from multiple partner neurons. Since the mere observation of spatial clusters does not demonstrate their functional relevance, we searched through the parameter space of the clustering algorithm to find parameter values that resulted in clusters in which the participating neurons shared commonalities in their activity during various behaviors. In all but one trial, parameter ranges could be identified for which spatial clusters indeed corresponded to functional groupings (Fig. 8b). We used a least-squares fit approach to find the location in parameter space of the strongest correspondence (Fig. 8c, Fig. S3, and Methods). In the two swim trials, the peaks were located at $d_{\mathrm{ext}} = 61 \pm 2$ µm and 65 ± 2 µm respectively; in the two crawl trials at 14 ± 5 µm and 18 ± 3 µm. In summary, functionally relevant spatial clusters during swimming were governed by very different parameter values than during crawling.

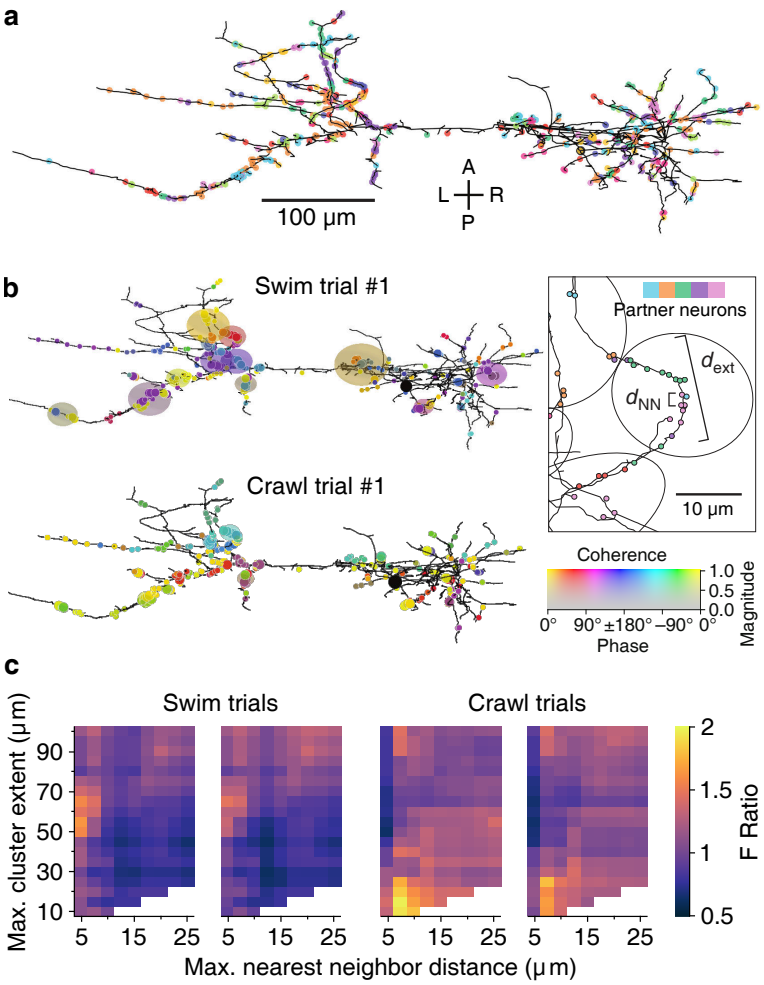

Figure 8: Synaptic clustering. **a**. Tracing of DE-3^{R} with synapses (arbitrarily) colored by presynaptic partner. **b**. Synaptic clusters obtained with parameter values (d_{NN}, d_{ext}) = (5 µm, 65 µm) and (d_{NN}, d_{ext}) = (7.5 µm, 15 µm) for swimming (*top*) and crawling (*bottom*), respectively. Here, synapses are colored by the coherence between the activity of their presynaptic partner and DE-3^{R} during the behaviors (as in Fig. 1). Clusters (elliptic areas) are colored by the average coherence of their constituent presynaptic partners. Inset: Explanation of clustering parameters (see Methods). **c**. All clustering results for swim and crawl trials. Color indicates the degree of correspondence between spatial clusters and functional grouping expressed as an F-ratio from complex ANOVA (see Methods) as a function of clustering parameters.

Discussion

We combined voltage-sensitive dye imaging with serial blockface electron microscopy to obtain a comprehensive recording of neuronal activity at the scale of an entire leech ganglion along with a full record of the anatomy of that same ganglion.

The use of a fast and sensitive VSD (Woodford et al., 2015) allowed us to record even small membrane potential fluctuations from somata. Those signals included both subthreshold excitatory and inhibitory synaptic potentials that could not have been detected by calcium imaging.

Conversely, SBEM (Lippens et al., 2019) allowed us to image the entire neuropil with sufficient resolution to visualize even thin neurites through much of the volume.

Within this vast dataset, we have focused on a neuron that plays three very distinct dynamic roles in different behaviors: motor neuron DE-3^{R}, a main excitatory motor neuron of the dorsal longitudinal muscle, as well as its presynaptic partners (Stent et al., 1978). We reconstructed its entire arborization and traced all of its presynaptic partners back to their somata. Thus, we generated a detailed map of the output stage of a multifunctional circuit that controls many of the animal's main forms of gross body movement, including swimming, crawling, and the local bend escape.

The reconstructed morphology of DE-3^{R} was in accordance with previous light microscopic studies in adult (Norris and Calabrese, 1987; Fan et al., 2005) and electron microscopy in a juvenile ganglion (Pipkin et al., 2016): its primary neurite emerged from the soma laterally and traveled toward the ipsilateral roots before making a 180° turn to run laterally across the ganglion. Our tracing revealed 531 synapses onto DE-3^{R}. This was slightly lower than the number previously reported for a juvenile ganglion (650) (Pipkin et al., 2016). The difference may be due to individual variability or developmental plasticity. Several of the synapses we found were with presynaptic partners that had previously been reported (Ort et al., 1974; Wagenaar, 2017) based on paired electrophysiological recordings. We focused here on chemical synaptic connections, since SBEM does not yet allow for the identification of gap junctions. However, electrical synapses between DE-3^{R} and their contralateral homologs as well as some interneurons do exist (Fan et al., 2005). Work on molecular markers of electrical synapses that do not require expression of a particular connexin (Shu et al., 2011) may overcome this hurdle in the foreseeable future.

The activity patterns observed during all three fictive behaviors exhibited by the single leech in this study (Figs. 1, 2, and 3) matched observations from a larger group of animals reported before Tomina and Wagenaar (2017): The majority of neurons in the ganglion were phasically active during multiple behaviors, indicating considerable but not complete overlap between the circuits that govern the behaviors (Briggman and Kristan, 2006). We conclude that the leech used in this study was representative of its species.

Overlaying the anatomical and activity images (Fig. 4) and comparing with the established canonical maps of the ganglion (Wagenaar, 2017) allowed us to address form–function relationships. For instance: Our own data allowed us to ask whether neurons that are more strongly associated with a particular behavior than with others formed synapses onto the output motor neuron that were spatially localized. Such an arrangement would indicate a modular organization of the motor neuron's processes (London and Häusser, 2005). However, we found no evidence of such organization in DE-3^{R} (Fig. 7d, e). We also asked whether synapses with a particular valence (excitatory or inhibitory) were differently distributed along the tree, which would likewise have implications for possible models of computation in the cell (Saha and Truccolo, 2019). Thanks to an extensive body of previously published electrophysiological recordings from the leech ganglion, the valence of many of DE-3^{R}'s presynaptic partners is known, allowing us to visualize the spatial

distributions of excitatory and inhibitory synapses separately (Fig. 7b). However, we found no obvious differences between the two classes of synapses (Fig. 7c).

The lack of macroscopic organization of functionally related synapses does not imply that the spatial arrangement of synapses on the tree has no functional relevance. Indeed, the limited experimental evidence currently available suggests that even clusters of two synapses are functionally relevant in the mammalian cortex (Takahashi et al., 2012; Fu et al., 2012). We therefore applied a spatial clustering algorithm to the input synapses on DE-3^R and asked whether the clusters identified by that algorithm also stand out as functionally significant groupings. Indeed, we found a set of parameter values for which synapses within spatial clusters also clustered in the phase space of the swim rhythm and a different set of parameters for which synapses within spatial clusters also clustered in the phase space of the crawl rhythm (Fig. 8b, c). Results were highly consistent between trials of the same behavior. (The results of clustering were not consistent among local bending trials. This may stem from a nature of this reflex behavior: there are variability of responsiveness of population of neurons involving pressure sensation, which can reflect plasticity of the reflex circuit (Crisp and Burrell, 2009).) In agreement with earlier reports (Kleindienst et al., 2011), the strongest correspondence between spatial clusters and activity patterns was observed when synaptic clusters were defined by a maximum distance between nearest neighbors (d_{NN}) of up to 10 μm. In contrast to earlier work that relied on light microscopy and could therefore not identify presynaptic partners, our use of SBEM allowed us to base our assessment directly on individually identified synapses. An attractive interpretation of our results is that the clusters are the loci where inputs from synchronized presynaptic cell assemblies are integrated (Briggman and Kristan, 2008).

To more fully understand the mechanisms underlying synaptic integration in motor neurons like DE-3^R, additional studies are required to complement our data. For instance, single-cell voltage imaging (Kuhn and Roome, 2019) and voltage clamp using sharp electrodes on neurites (Laurent, 1993; Takashima et al., 2006) would help determine where in the neurites active propagation of membrane potentials is supported and thus lead to a better understanding of how postsynaptic potentials as well as action potentials propagate through the tree. As it stands, we only have voltage data from the soma. Leech neurons—along with most neurons in the central nervous systems of other annelids, arthopods, and molluscs—have a unipolar morphology with the somata strictly segregated from neuropil (Bullock and Horridge, 1965). With notable exceptions (including sensory neurons in the leech and select insect motorneurons (Hancox and Pitman, 1992)), these somata are thought to play a relatively minor role in the integration of synaptic inputs to action potential outputs (Andjelic and Torre, 2005).

Even so, the completeness of our functional dataset in combination with our anatomical data makes for an attractive basis for simulation studies to arrive at a computational understanding of multifunctional neuronal circuits (Real et al., 2017). Our data may also serve as a large-scale ground truth for EM segmentation algorithms (Plaza and Funke, 2018). This study not only represents an important step in a combined approach to studying multifunctional circuits at the synaptic level, but also lays the groundwork for a comprehensive neuronal mapping of a whole ganglion

that semi-autonomously processes local sensory information and controls segmental movement.

The combination of anatomical methods with synaptic resolution and imaging techniques that can record from the entirety of the neurons of a circuit promises an extraordinary opportunity to assess neural computations at the level of circuit dynamics. Functional maps (Alivisatos et al., 2012) from recorded activity combined with anatomical connectomes (Denk et al., 2012; Bargmann and Marder, 2013; Morgan and Lichtman, 2013) are therefore poised to become a powerful tool not only to have a better understanding of complex behaviors, but also to predict the outcomes of new manipulations Devor et al. (2013); Kandel et al. (2013); Wang et al. (2013). This new addition with the annelid species to the developing field would also pave the way for comparative approaches by functional connectomics to study evolutionary aspects of neuronal design (Laurent, 2020).

Materials and methods

Dissection and voltage-sensitive dye imaging

Detailed procedures have been described before (Tomina and Wagenaar, 2018). Briefly, leeches (*Hirudo verbana*, obtained from Niagara Leeches, Niagara Falls, NY) were maintained on a 12h:12h light:dark cycle in temperature-controlled aquariums filled with artificial pond water. The entire nervous system of a leech was removed and pinned down on silicone (PDMS, Sylgard 184, Dow Corning, Midland, MI). The sheath surrounding one segmental ganglion (M10) was removed from both ventral and dorsal aspects to allow access with voltage-sensitive dyes. Most of the nerves that innervate the periphery were cut short, but several were kept long to allow extracellular stimulation as described before Tomina and Wagenaar (2017). A voltage-sensitive dye (VF2.1(OMe).H (Woodford et al., 2015) provided by Evan Miller) was bath-loaded at a concentration of 800 nM in leech saline using a pair of peristaltic pumps to evenly load cell membranes on both sides of the ganglion. The preparation was placed on a custom-built dual-headed microscope which was used to image neuronal activity during fictive behaviors triggered by electrical stimulation, as in our previous work (Tomina and Wagenaar, 2017).

We manually drew regions of interest (ROIs) around neuronal cell bodies and used custom software to associate those ROIs with named cells on the canonical maps of the leech ganglion Wagenaar (2017). For each of the behavior trials separately, we calculated the spectral coherence between each of the neurons and DE-3^R at the frequency of the dominant peak in the power spectrum of DE-3^R for the given behavior.

Histology

After dye imaging, the preparation was reduced to just one segmental ganglion by transecting the anterior and posterior connectives. The ganglion was mounted on a slab of silicone (DPMS) with a hole cut out in the center so that the somata would not be in direct contact with the silicone. This preparation was transferred into a glass container and incubated for 72 hours at 4 °C in

2% paraformaldehyde, 2.5% glutaraldehyde in 0.15 M cacodylate buffer containing 2 mM $CaCl_2$. Subsequently, the ganglion was washed in cacodylate buffer for 10 minutes and then incubated in an aqueous solution of 2% OsO_4 and 1.5% potassium ferrocyanide. During this incubation, the sample was microwaved in a scientific microwave (Pelco 3440 MAX) three times at 800 W with a duty cycle of 40 seconds on and 40 seconds off at a controlled temperature of 35 °C and subsequently left at room temperature (RT) for 30 minutes. The sample was then washed twice in ddH_2O and then microwaved three times at 30 °C with a duty cycle of 2 minutes on and 2 minutes off.

The sample was incubated in 0.5% thiocarbohydrazide (Electron Microscopy Sciences, Hatfield, PA). During this incubation, the sample was microwaved three times at 800 W with a duty cycle of 40 seconds on and 40 seconds off at 30 °C and subsequently left at RT for 15 minutes. The ganglion was then washed again, followed by the same microwave incubation as described above.

Next, the sample was incubated in 2% aqueous OsO_4, microwaved three times at 800 W with a duty cycle of 40 seconds on and 40 seconds off at 30 °C, and left for 30 minutes at RT. After another wash, the sample was left overnight in 2% uranyl acetate at 4 °C.

The next day, the sample was incubated in a lead aspartate solution at 60 °C for 25 minutes Walton (1979). The sample was then washed and dehydrated through a series of ethanol solutions (50%, 70%, 90%, 100%, 100%, 10 minutes each) at RT and incubated in acetone. After this, the sample was infiltrated with epoxy resin by first incubating it for one day at RT in a solution of 25% Durcupan (Sigma, St. Louis, MO) in acetone. On subsequent days, the concentration of Durcupan was increased to 50%, 75%, and finally 100%. After that, the sample was transferred to freshly prepared 100% Durcupan and incubated at 60 °C for 3 days.

Micro-CT Imaging

We used Micro-CT scanning to confirm that the above sample preparation had left the overall geometry of the ganglion intact and to trace portions of neurons outside of the neuropil. Scans were collected using the 20x objective on a Zeiss Versa 510 X-ray microscope. Epoxy-embedded ganglia were attached to the end of an aluminum rod using cyanoacrylate glue and then scanned at 80 kV, collecting 2401 projection images while rotating the specimen 360 degrees. The final pixel size was approximately 0.75 μm. Volumes were reconstructed using Zeiss Reconstructor software and visualized in custom software (GVox, see "Data availability").

Scanning electron microscopy

Ganglia were mounted onto aluminum pins using conductive silver paint. The ganglia were mounted in a vertical orientation (with the anterior connective pointing upwards). The sample was imaged with a Zeiss Gemini 300 SEM with a Gatan 2XP 3View system. The microscope was run in focal charge compensation mode (Deerinck et al., 2018) using nitrogen gas (40% pressure),

with an accelerating voltage of 2.5 kV, a 30 μm objective aperture, magnification of 336x, a raster size of 17100 × 17100 pixels, a 5.5 nm pixel size, a 0.5 μs dwell time, and 50 nm section thickness. Stage montaging with an overlap of 8% between tiles was used to cover the complete extent of the ganglion in any given image. The backscatter detector was a Hamamatsu diode with a 2-mm aperture.

Outside of the neuropil, neuronal processes could be traced in the micro-CT scan, which allowed us to reduce the total volume needed to be imaged with SBEM by almost a factor two (Figure 4b). Still, at the widest points of the neuropil as many as 7 × 2 tiles (119,700 × 34,200 pixels) were needed at a given z-position.

After approximately every 500 sections, the run was stopped to clear sectioning debris from the diamond knife and prevent contamination of the block-face, diode, or column. The run was also stopped when we reached significantly wider or narrower regions of the neuropil as indicated above. Ultimately, the run was subdivided into 61 subruns. There was only one instance in the run where a significant loss of tissue occurred (approximately 150 nm) following the re-approach of the knife to the tissue after an interruption for clearing debris. Overall, electron microscopy took nearly 7 months of near continuous imaging.

Transmission electron microscopy

Image quality and specimen preservation were verified using an additional ganglion prepared as above, but imaged in ultrathin sections on a conventional transmission electron microscope (JEOL JEM-1200EX, 120 kV, 12,000x–20,000x magnification).

Image processing

Images were aligned using custom software. First, we reduced the linear resolution of the original images by a factor five. Then we split each image into 5x5 sub-tiles and calculated the optimal alignment between each sub-tile and the corresponding sub-tile from the image above using a modified version of SWIFT-IR (Wetzel et al., 2016). Likewise, we split the regions of overlap that existing between images of the same slice into 5 sub-tiles and calculated the optimal alignment between the edges of adjacent images. We used these latter numbers to coarsely align images within each slice and render the first and last slices of each subrun at 1:25 scale, which allowed us to establish regions of correspondence between subruns. Using these procedures, we ended up with 3,430,650 matching pairs of image locations. Because SWIFT-IR matches up entire areas rather than single point pairs, those locations are defined at a much higher resolution than that of the images. Accordingly, alignment information obtained at a scale of 1:5 could be used to align the source images at scale 1:1 without material loss of precision.

Next, we split the full EM volume up into subvolumes of 200 slices with 50% overlap between subsequent subvolumes (Stefan Saalfeld, personal communication) and optimized alignment in each subvolume independently. This was done in three steps: (1) Coarse alignment of all the z-

stacks from all of the subruns involved in the subvolume relative to each other; (2) Refinement of this alignment by determining optimal rigid translation of each tile relative to its substack; (3) Further refinement through elastic deformation. This procedure resulted in absolute coordinates for a grid of points in each source image.

We then rendered each slice by linearly combining the placement according to the two subvolumes that incorporated the slice. We divided each slice up into nonoverlapping rectangles and rendered pixels from one source image into each rectangle using a perspective transformation derived from the grid coordinates calculated in the previous step.

The full-resolution stitched volume was then split into tiles of 512x512x1 voxels and reduced-resolution tiles at 1:2, 1:4, up to 1:256 resolution were produced for faster online visualization.

Visualization

We developed a custom tool for visualizing the aligned images and for neurite tracing. SBEMViewer (see "Data availability") was used to visualize the slices as they came off the microscope to monitor image quality, and also for purposes of tracing neurites.

Neurite tracing

We produced a full skeleton tracing of the right DE-3 motor neuron and all of its presynaptic partners from the synapses to their somata. The following criteria were used to identify synapses:

1. Vesicles have to be evident on the presynaptic site;
2. Those vesicles have to be in immediate proximity of the putative synapse;
3. The pre- and postsynaptic cells must have membrane apposition across at least three sections (150 nm).

Because of limited resolution in our SBEM images, synaptic vesicles appear merely as gray granules (Fig. 5c,d), but fields of such granules were clearly distinct from other gray areas in the SBEM images. Comparison with digitally blurred TEM images (Fig. S1) confirmed this interpretation. We found that granular areas were concentrated in fiber endings and varicosities.

Synaptic clustering analysis

The analysis was based on data from the 45 synaptic partners of DE-3^{R} for which both anatomical as well as VSD recordings were available. We defined synaptic clusters using an agglomerative hierarchical clustering algorithm with two parameters:

(1) The maximum allowed distance between nearest neighbors (d_{NN});

(2) The maximum overall spatial extent of the cluster (d_{ext}).

The algorithm began by treating each synapse as an individual cluster. Then, it iteratively joined the two clusters with minimum distance between their most proximal elements ("single-linkage" clustering). However, if a joint cluster would exceed the limit on overall spatial extent (d_{ext}), its putative constituents were not joined. Aggregation stopped when no pairs of clusters were left with acceptable nearest-neighbor distance (i.e., less than d_{NN}) and acceptable joint spatial extent (i.e., less than d_{ext}). All distances were measured along the neurites of DE-3$^{\mathrm{R}}$ rather than by Euclidean metric in the volume. We explored maximum nearest-neighbor distances between 5 and 25 μm, and maximum spatial extents between 10 and 100 μm. Clusters comprising only a single synapse were not considered for further analysis.

The analysis of functional significance of spatial clusters used an ANOVA-like procedure on the complex spectral coherence values of neurons within clusters relative to DE-3$^{\mathrm{R}}$. As in ANOVA, we calculated sums of squares within and between clusters. Since coherence values are complex numbers, we used the *absolute* square value. In standard ANOVA, the ratio of these sums of squares (the "F-ratio") follows an F-distribution under the null hypothesis. In the complex-valued case, that is no longer true, so we calculated empirical distributions of the F-ratios by randomly shuffling the list of per-neuron coherence values 1000 times. The empirical p-value $\hat{p}$ was then defined as $\hat{p} = \frac{m+1}{N+1}$, where $N = 1000$ is the number of randomizations and m is the number of times the F-ratio from shuffled data exceeded the experimentally observed F-ratio. These p-values are reported in the supplemental tables.

We generated plots of the F-ratio as a function of the cluster parameters d_{NN} and d_{ext}. For each trial, we first determined the value of d_{NN} for which the largest F-ratio was obtained. Then, we fitted a Gaussian of the form

$$F = 1 + A \exp\left(-\frac{1}{2}[d_{\mathrm{ext}} - \mu]^2/\sigma^2\right)$$

to the F-ratio as a function of d_{ext} (Fig. S3). The μ-values from those fits and their uncertainties according to least-squares fitting are reported in the text.

References

Ahrens MB, Orger MB, Robson DN, Li JM, and Keller PJ, 2013. Whole-brain functional imaging at cellular resolution using light-sheet microscopy. *Nat Methods* **10** (5): 413–420. PMID 23524393.

Alivisatos AP, Chun M, Church GM, Greenspan RJ, Roukes ML, and Yuste R, 2012. The brain activity map project and the challenge of functional connectomics. *Neuron* **74** (6): 970–974. PMID 22726828.

Andjelic S and Torre V, 2005. Calcium dynamics and compartmentalization in leech neurons. *J Neurophysiol* **94** (6): 4430–4440. PMID 16135547.

Bargmann CI and Marder E, 2013. From the connectome to brain function. *Nat Methods* **10** (6): 483–490.

Bates AS, Schlegel P, Roberts RJV, Drummond N, Tamimi IFM, Turnbull R, Zhao X, Marin EC, Popovici PD, Dhawan S, Jamasb A, Javier A, Li F, Rubin GM, Waddell S, Bock DD, Costa M, and Jefferis GSXE, 2020. Complete connectomic reconstruction of olfactory projection neurons in the fly brain. *Biorxiv*: https://doi.org/10.1101/2020.01.19.911453.

Bedny M, Richardson H, and Saxe R, 2015. "Visual" Cortex Responds to Spoken Language in Blind Children. *J Neurosci* **35** (33): 11674–11681. PMID 26290244.

Bhattacharya A, Aghayeva U, Berghoff EG, and Hobert O, 2019. Plasticity of the Electrical Connectome of C. elegans. *Cell* **176** (5): 1174–1189. PMID 30686580.

Bock DD, Lee WC, Kerlin AM, Andermann ML, Hood G, Wetzel AW, Yurgenson S, Soucy ER, Kim HS, and Reid RC, 2011. Network anatomy and in vivo physiology of visual cortical neurons. *Nature* **471** (7337): 177–182. PMID 21390124.

Briggman KL, Abarbanel HDI, and Kristan WB, 2005. Optical imaging of neuronal populations during decision-making. *Science* **307** (5711): 896–901. PMID 15705844.

Briggman KL, Helmstaedter M, and Denk W, 2011. Wiring specificity in the direction-selectivity circuit of the retina. *Nature* **471** (7337): 183–188. PMID 21390125.

Briggman KL and Kristan WB, 2008. Multifunctional pattern-generating circuits. *Annu Rev Neurosci* **31**: 271–294. PMID 18558856.

Briggman KL and Kristan Jr WB, 2006. Imaging dedicated and multifunctional neural circuits generating distinct behaviors. *J Neurosci* **26** (42): 10925–10933. PMID 17050731.

Bullock TH and Horridge GA, 1965. *Structure and function in the nervous systems of invertebrates*. W. H. Freeman, San Francisco.

Bushong EA, Johnson Jr DD, Kim KY, Terada M, Hatori M, Peltier ST, Panda S, Merkle A, and Ellisman MH, 2015. X-ray microscopy as an approach to increasing accuracy and efficiency of serial block-face imaging for correlated light and electron microscopy of biological specimens. *Microsc Microanal* **21** (1): 231–238. PMID 25392009.

Carr CE and Konishi M, 1988. Axonal delay lines for time measurement in the owl's brainstem. *Proc Natl Acad Sci U S A* **85** (21): 8311–8315. PMID 3186725.

Crisp KM and Burrell BD, 2009. Cellular and behavioral properties of learning in leech and other annelids. In DH Shain (ed.), *Annelids in Modern Biology*, 133–155. Wiley-Blackwell.

de Boer P, Hoogenboom JP, and Giepmans BN, 2015. Correlated light and electron microscopy: ultrastructure lights up! *Nat Methods* **12** (6): 503–513. PMID 26020503.

Deerinck TJ, Shone TM, Bushong EA, Ramachandra R, Peltier ST, and Ellisman MH, 2018. High-performance serial block-face SEM of nonconductive biological samples enabled by focal gas injection-based charge compensation. *J Microsc* **270** (2): 142–149. PMID 29194648.

Denk W, Briggman KL, and Helmstaedter M, 2012. Structural neurobiology: missing link to a mechanistic understanding of neural computation. *Nature Rev Neurosci* **13** (5): 351–358. PMID 22353782.

Devor A, Bandettini PA, Boas DA, Bower JM, Buxton RB, Cohen LB, Dale AM, Einevoll GT, Fox PT, Franceschini MA, Friston KJ, Fujimoto JG, Geyer MA, Greenberg JH, Halgren E, Hamalainen MS, Helmchen F, Hyman BT, Jasanoff A, Jernigan TL, Judd LL, Kim SG, Kleinfeld D, Kopell NJ, Kutas M, Kwong KK, Larkum ME, Lo EH, Magistretti PJ, Mandeville JB, Masliah E, Mitra PP, Mobley WC, Moskowitz MA, Nimmerjahn A, Reynolds JH, Rosen BR, Salzberg BM, Schaffer CB, Silva GA, So PT, Spitzer NC, Tootell RB, Van Essen DC, Vanduffel W, Vinogradov SA, Wald LL, Wang LV, Weber B, and Yodh AG, 2013. The challenge of connecting the dots in the B.R.A.I.N. *Neuron* **80** (2): 270–274. PMID 24139032.

Eichler K, Li F, Litwin-Kumar A, Park Y, Andrade I, Schneider-Mizell CM, Saumweber T, Huser A, Eschbach C, Gerber B, Fetter RD, Truman JW, Priebe CE, Abbott LF, Thum AS, Zlatic M, and Cardona A, 2017. The complete connectome of a learning and memory centre in an insect brain. *Nature* **548** (7666): 175–182. PMID 28796202.

Eschbach C, Fushiki A, Winding M, Schneider-Mizell CM, Shao M, Arruda R, Eichler K, Valdes-Aleman J, Ohyama T, Thum AS, Gerber B, Fetter RD, Truman JW, Litwin-Kumar A, Cardona A, and Zlatic M, 2020. Recurrent architecture for adaptive regulation of learning in the insect brain. *Nat Neurosci* **23** (4): 544–555. PMID 32203499.

Fan RJ, Marin-Burgin A, French KA, and Friesen WO, 2005. A dye mixture (Neurobiotin and Alexa 488) reveals extensive dye-coupling among neurons in leeches; physiology confirms the connections. *J Comp Physiol A* **191** (12): 1157–1171. PMID 16133497.

Fu M, Yu X, Lu J, and Zuo Y, 2012. Repetitive motor learning induces coordinated formation of clustered dendritic spines in vivo. *Nature* **483** (7387): 92–95. PMID 22343892.

Galvez-Pol A, Forster B, and Calvo-Merino B, 2018. Modulation of motor cortex activity in a visual working memory task of hand images. *Neuropsychologia* **117**: 75–83. PMID 29738793.

Google, 2016. Neuroglancer: WebGL-based viewer for volumetric data. URL `https://github.com/google/neuroglancer`.

Grinvald A and Hildesheim R, 2004. VSDI: a new era in functional imaging of cortical dynamics. *Nature Rev Neurosci* **5** (11): 874–885. PMID 15496865.

Hancox JC and Pitman RM, 1992. A time-dependent excitability change in the soma of an identified insect motoneurone. *J Exp Biol* **162**: 251–263.

Harris KM, Perry E, Bourne J, Feinberg M, Ostroff L, and Hurlburt J, 2006. Uniform serial sectioning for transmission electron microscopy. *J Neurosci* **26** (47): 12101–12103. PMID 17122034.

Hildebrand DGC, Cicconet M, Torres RM, Choi W, Quan TM, Moon J, Wetzel AW, Champion AS, Graham BJ, Randlett O, Plummer GS, Portugues R, Bianco IH, Saalfeld S, Baden AD, Lillaney K, Burns R, Vogelstein JT, Schier AF, Lee WA, Jeong WK, Lichtman JW, and Engert F, 2017. Whole-brain serial-section electron microscopy in larval zebrafish. *Nature* **545** (7654): 345–349. PMID 28489821.

Jiao ZF, Shang CF, Wang YF, Yang Z, Yang C, Li FN, Xie JZ, Pan JW, Fu L, and Du JL, 2018. All-optical imaging and manipulation of whole-brain neuronal activities in behaving larval zebrafish. *Biomed Opt Express* **9** (12): 6154–6169. PMID 31065420.

Kandel ER, Markram H, Matthews PM, Yuste R, and Koch C, 2013. Neuroscience thinks big (and collaboratively). *Nature Rev Neurosci* **14** (9): 659–664. PMID 23958663.

Kleindienst T, Winnubst J, Roth-Alpermann C, Bonhoeffer T, and Lohmann C, 2011. Activity-dependent clustering of functional synaptic inputs on developing hippocampal dendrites. *Neuron* **72** (6): 1012–1024. PMID 22196336.

Kristan Jr WB, Calabrese RL, and Friesen WO, 2005. Neuronal control of leech behavior. *Prog Neurobiol* **76** (5): 279–327. PMID 16260077.

Kuhn B and Roome CJ, 2019. Primer to Voltage Imaging With ANNINE Dyes and Two-Photon Microscopy. *Front Cell Neurosci* **13**: 321. PMID 31379507.

Kulkarni RU and Miller EW, 2017. Voltage Imaging: Pitfalls and Potential. *Biochemistry* **56** (39): 5171–5177. PMID 28745864.

Laurent G, 1993. A dendritic gain control mechanism in axonless neurons of the locust, Schistocerca americana. *J Physiol* **470**: 45–54. PMID 8308737.

Laurent G, 2020. On the value of model diversity in neuroscience. *Nature Rev Neurosci* **21** (8): 395–396. PMID 32514109.

Lippens S, Kremer A, Borghgraef P, and Guérin CJ, 2019. Serial block face-scanning electron microscopy for volume electron microscopy. *Methods Cell Biol* **152**: 69–85. PMID 31326027.

London M and Häusser M, 2005. Dendritic computation. *Annu Rev Neurosci* **28**: 503–532. PMID 16033324.

Macagno ER, 1980. Number and distribution of neurons in leech segmental ganglia. *J Comp Neurol* **190** (2): 283–302. PMID 7381060.

Maniates-Selvin JT, Hildebrand DGC, Graham BJ, Kuan AT, Thomas LA, Nguyen T, Buhmann J, Azevedo AW, Shanny BL, Funke J, Tuthill JC, and Lee WCA, 2020. Reconstruction of motor control circuits in adult Drosophila using automated transmission electron microscopy. *Biorxiv*: https://doi.org/10.1101/2020.01.10.902478.

Miroschnikow A, Schlegel P, Schoofs A, Hueckesfeld S, Li F, Schneider-Mizell CM, Fetter RD, Truman JW, Cardona A, and Pankratz MJ, 2018. Convergence of monosynaptic and polysynaptic sensory paths onto common motor outputs in a Drosophila feeding connectome. *Elife* **7**: 10.7554/eLife.40247 [doi]; e40247. PMID 30526854.

Morgan JL and Lichtman JW, 2013. Why not connectomics? *Nat Methods* **10** (6): 494–500. PMID 23722208.

Muller KJ and McMahan UJ, 1976. The shapes of sensory and motor neurones and the distribution of their synapses in ganglia of the leech: a study using intracellular injection of horseradish peroxidase. *Proc Roy Soc Lond B* **194** (1117): 481–499. PMID 12513.

Muller KJ, Nicholls JG, and Stent GS (eds.), 1981. *Neurobiology of the leech*. Cold Spring Harbor Laboratory Press, Cold Spring Harbor, NY.

Norris BJ and Calabrese RL, 1987. Identification of motor neurons that contain a FMRFamidelike peptide and the effects of FMRFamide on longitudinal muscle in the medicinal leech, *Hirudo medicinalis*. *J Comp Neurol* **266** (1): 95–9111. PMID 3323268.

Ogawa H, Kawakami Z, and Yamaguchi T, 1995. Motor pattern of the stinging response in the honeybee Apis mellifera. *J Exp Biol* **198**: 39–47. PMID 9317296.

Ort CA, Kristan WB, and Stent GS, 1974. Neuronal control of swimming in medicinal leech. 2. Identification and connections of motor neurons. *J Comp Physiol* **94** (2): 121–154.

Pipkin JE, Bushong EA, Ellisman MH, and Kristan Jr WB, 2016. Patterns and distribution of presynaptic and postsynaptic elements within serial electron microscopic reconstructions of neuronal arbors from the medicinal leech *Hirudo verbana*. *J Comp Neurol* **524** (18): 3677–3695. PMID 27636374.

Plass J, Ahn E, Towle VL, Stacey WC, Wasade VS, Tao J, Wu S, Issa NP, and Brang D, 2019. Joint Encoding of Auditory Timing and Location in Visual Cortex. *J Cogn Neurosci* **31** (7): 1002–1017. PMID 30912728.

Plaza SM and Funke J, 2018. Analyzing Image Segmentation for Connectomics. *Front Neural Circuits* **12**: 102. PMID 30483069.

Real E, Asari H, Gollisch T, and Meister M, 2017. Neural Circuit Inference from Function to Structure. *Curr Biol* **27** (2): 189–198. PMID 28065610.

Saha D and Truccolo W, 2019. Stochastic point process models for multi-compartment dendritic-tree input-output transformations in spiking neurons. *Conf Proc IEEE Eng Med Biol Soc* **2019**: 4395–4399. PMID 31946841.

Scholl B, Thomas CI, Ryan MA, Kamasawa N, and Fitzpatrick D, 2019. Cortical neuron response selectivity derives from strength in numbers of synapses. *bioRxiv*: 2019.12.24.887422. URL `https://doi.org/10.1101/2019.12.24.887422`.

Shu X, Lev-Ram V, Deerinck TJ, Qi Y, Ramko EB, Davidson MW, Jin Y, Ellisman MH, and Tsien RY, 2011. A genetically encoded tag for correlated light and electron microscopy of intact cells, tissues, and organisms. *PLoS Biol* **9** (4): e1001041. PMID 21483721.

Stent GS, Kristan Jr WB, Friesen WO, Ort CA, Poon M, and Calabrese RL, 1978. Neuronal generation of the leech swimming movement. *Science* **200** (4348): 1348–1357. PMID 663615.

Takahashi N, Kitamura K, Matsuo N, Mayford M, Kano M, Matsuki N, and Ikegaya Y, 2012. Locally synchronized synaptic inputs. *Science* **335** (6066): 353–356. PMID 22267814.

Takashima A, Hikosaka R, and Takahata M, 2006. Functional significance of passive and active dendritic properties in the synaptic integration by an identified nonspiking interneuron of crayfish. *J Neurophysiol* **96** (6): 3157–3169. PMID 16914611.

Tomina Y and Wagenaar DA, 2017. A double-sided microscope to realize whole-ganglion imaging of membrane potential in the medicinal leech. *Elife* **6**: e29839. PMID 28944754.

Tomina Y and Wagenaar DA, 2018. Dual-sided voltage-sensitive dye imaging of leech ganglia. *Bio Protoc* **8** (5): e2751. PMID 29594188.

Varga Z, Jia H, Sakmann B, and Konnerth A, 2011. Dendritic coding of multiple sensory inputs in single cortical neurons in vivo. *Proc Natl Acad Sci U S A* **108** (37): 15420–15425. PMID 21876170.

Vishwanathan A, Daie K, Ramirez AD, Lichtman JW, Aksay ERF, and Seung HS, 2017. Electron Microscopic Reconstruction of Functionally Identified Cells in a Neural Integrator. *Curr Biol* **27** (14): 2137–2147. PMID 28712570.

Wagenaar DA, 2015. A classic model animal in the 21st century: recent lessons from the leech nervous system. *J Exp Biol* **218** (21): 3353–3359. PMID 26538172.

Wagenaar DA, 2017. An interactive map of the segmental ganglia of *Hirudo verbana*. URL `http://wagenaarlab.caltech.edu/ganglion`, retrieved Feb 10, 2020.

Walton J, 1979. Lead aspartate, an en bloc contrast stain particularly useful for ultrastructural enzymology. *J Histochem Cytochem* **27** (10): 1337–1342. PMID 512319.

Wang Z, Chen LM, Negyessy L, Friedman RM, Mishra A, Gore JC, and Roe AW, 2013. The relationship of anatomical and functional connectivity to resting-state connectivity in primate somatosensory cortex. *Neuron* **78** (6): 1116–1126. PMID 23791200.

Wanner AA and Friedrich RW, 2020. Whitening of odor representations by the wiring diagram of the olfactory bulb. *Nat Neurosci* **23** (3): 433–442. PMID 31959937.

Wetzel AW, Bakal J, Dittrich M, Hildebrand DGC, Morgan HL, and Lichtman JW, 2016. Registering large volume serial-section electron microscopy image sets for neural circuit reconstruction using FFT signal whitening. In *Proc. IEEE Applied Imagery Pattern Recognition Workshop*, 10.1109/AIPR.2016.8010595.

Woodford CR, Frady EP, Smith RS, Morey B, Canzi G, Palida SF, Araneda RC, Kristan Jr WB, Kubiak CP, Miller EW, and Tsien RY, 2015. Improved PeT molecules for optically sensing voltage in neurons. *J Am Chem Soc* **137** (5): 1817–1824. PMID 25584688.

Xu CS, Januszewski M, Lu Z, Takemura SY, Hayworth KJ, Huang G, Shinomiya K, Maitin-Shepard J, Ackerman D, Berg S, Blakely T, Bogovic J, Clements J, Dolafi T, Hubbard P, Kainmueller D, Katz W, Kawase T, Khairy KA, Leavitt L, Li PH, Lindsey L, Neubarth N, Olbris DJ, Otsuna H, Troutman ET, Umayam L, Zhao T, Ito M, Goldammer J, Wolff T, Svirskas R, Schlegel P, Neace ER, Knecht Jr CJ, Alvarado CX, Bailey DA, Ballinger S, Borycz JA, Canino BS, Cheatham N, Cook M, Dreher M, Duclos O, Eubanks B, Fairbanks K, Finley S, Forknall N, Francis A, Hopkins GP, Joyce EM, Kim SJ, Kirk NA, Kovalyak J, Lauchie SA, Lohff A, Maldonado C, Manley EA, McLin S, Mooney C, Ndama M, Ogundeyi O, Okeoma N, Ordish C, Padilla N, Patrick C, Paterson T, Phillips EE, Phillips EM, Rampally N, Ribeiro C, Robertson MK, Rymer JT, Ryan SM, Sammons M, Scott AK, Scott AL, Shinomiya A, Smith C, Smith K, Smith NL, Sobeski MA, Suleiman A, Swift J, Takemura S, Talebi I, Tarnogorska D, Tenshaw E, Tokhi T, Walsh JJ, Yang T, Horne JA, Li F, Parekh R, Rivlin PK, Jayaraman V, Ito K, Saalfeld S, George R, Meinertzhagen I, Rubin GM, Hess HF, Scheffer LK, Jain V, and Plaza SM, 2020. A connectome of the adult Drosophila central brain. *Biorxiv*: https://doi.org/10.1101/2020.01.21.911859.

Zarin AA, Mark B, Cardona A, Litwin-Kumar A, and Doe CQ, 2019. A multilayer circuit architecture for the generation of distinct locomotor behaviors in Drosophila. *Elife* **8**: 10.7554/eLife.51781 [doi]; e51781. PMID 31868582.

Zheng Z, Lauritzen JS, Perlman E, Robinson CG, Nichols M, Milkie D, Torrens O, Price J, Fisher CB, Sharifi N, Calle-Schuler SA, Kmecova L, Ali IJ, Karsh B, Trautman ET, Bogovic JA, Hanslovsky P, Jefferis GSXE, Kazhdan M, Khairy K, Saalfeld S, Fetter RD, and Bock DD, 2018. A Complete Electron Microscopy Volume of the Brain of Adult Drosophila melanogaster. *Cell* **174** (3): 730–743. PMID 30033368.

Article and author information

Acknowledgments

We thank Evan Miller (Berkeley) for sharing of the VF2.1(OMe).H dye, Art Wetzel (Pittsburgh Supercomputer Center) and Tom Bartol (The Salk Institute) for many useful discussions about image alignment, and Tünde Magyar and Renáta Pop (University of Veterinary Medicine, Department of Anatomy and Histology, Budapest, Hungary) for help with TEM.

Funding

This work was supported by the National Institute of Neurological Disorders and Stroke (R01-NS094403 to DAW) and by the National Institute of General Medical Sciences (P41GM103412 in support of the National Center for Molecular Imaging Research to MHE). YT was supported by Japan Society for Promotion of Science (Overseas Research Fellowship, Research Fellowship for Young Scientists PD, 201800526 and Grant-in-Aid for Young Scientists, 19K16191). PKF was supported by the Swiss National Science Foundation (P2EZP3-181896).

Author contributions

Conceptualization: YT, PKF, MHE, WBK, DAW. Data curation: YT, DAW. Formal analysis: YT, MA, PKF, DAW. Funding acquisition: YT, PKF, MHE, WBK, DAW. Investigation: YT, MA, PKF, EAB. Methodology: All. Software: PKF, DAW. Supervision: MHE, DAW. Visualization: YT, MA, PKF, DAW. Writing—original draft: YT, MA. Writing—review and editing: YT, MA, PKF, DAW.

Competing interests

The authors declare no competing interests.

Data and materials availability

The easiest way to access the raw electrophysiology and voltage-dye data as well as the tracing results used in this paper is through a series of Python modules that we made available at `https://github.com/wagenadl/leechem-public`. Included in the package is a file called "demo.py" that demonstrates the use of the modules. Supplemental table S4 lists the available VSD trials.

The aligned EM volume may be accessed through the Neuroglancer (Google, 2016) instance at `https://leechem.caltech.edu` or by pointing SBEMViewer to `https://leechem.caltech.edu/emdata`.

The code used for alignment is available at `https://github.com/wagenadl/sbemalign`. Our visualization tools SBEMViewer and GVox are at `https://github.com/wagenadl/sbemviewer` and `https://github.com/wagenadl/gvox`.

Supplementary materials

Figs. S1 to S3; Movie S1; Tables S1 to S4.

SUPPLEMENTARY MATERIAL

Supplementary figures

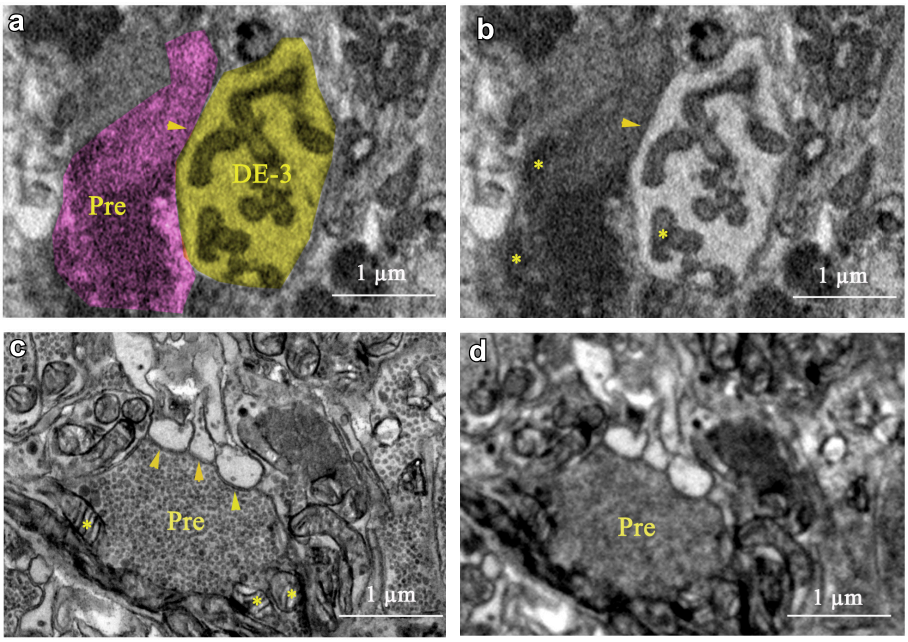

Figure S1: Comparison of SEM with TEM for interpreting synapses. **a**. Our interpretation of a small section of our SBEM image: a process of cell DE-3 (*yellow*) and a presynaptic partner (*purple*). **b**. Same area without overlay. *Arrowhead*: synapse. Stars: *Mitochondria*. **c**. A similar area imaged with TEM (from a ganglion from another leech). **d**. Same area as (c), computationally blurred to simulate the lower resolving power of SEM.

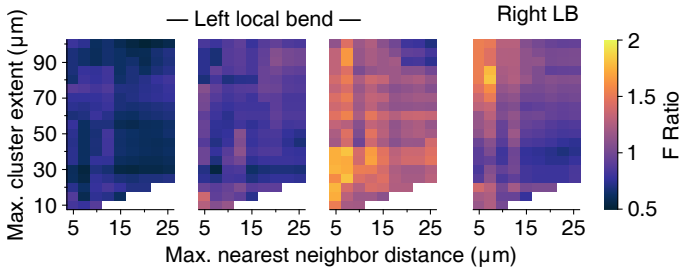

Figure S2: Clustering results for the local bend trials. Out of the four trials, the first three involved stimulation of the left P_V cell; the final trial involved stimulation of the right P_V cell. In contrast to the swim and crawl trials (7c), the clustering results for local bend trials are inconsistent.

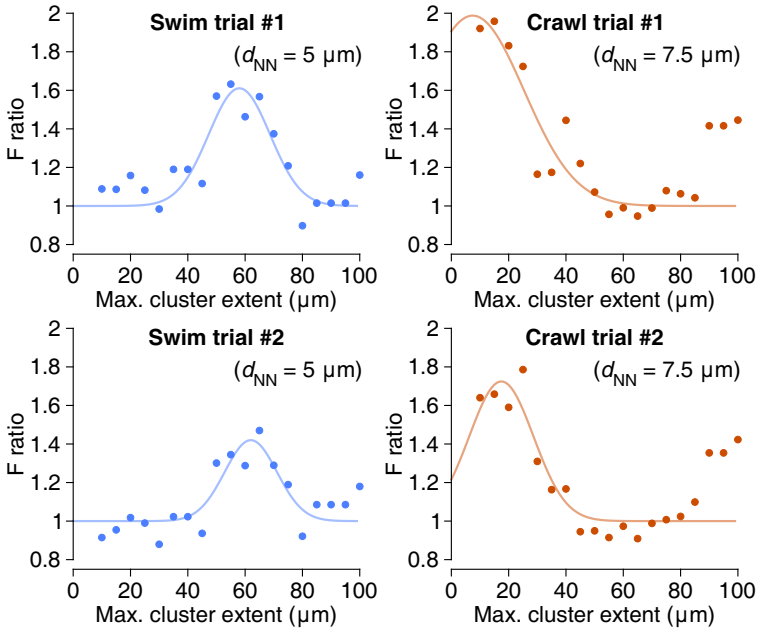

Figure S3: Peak F-ratios for connecting spatial clusters to functional activity. These graphs represent slices through the data shown in Fig. 8c, vertically through the highest peak in the parameter space. Lines are Gaussians fitted through the data; see Methods.

Supplementary movie

Movie S1. Full tracing of motor neuron DE-3^R with all of its input synapses, visualized growing out from the soma to the distal branches (0:00 to 0:05). Back tracings of all of DE-3^R's presynaptic partners to their somata (0:05 to 0:12). Rotational view of the completed tracing (0:12 to 0:15).

Supplementary tables

Table S1: Results of the ANOVA analysis of synaptic clusters in swim trials. Shown are all parameter values that resulted in a significant link between anatomy and activity ($p < 0.05$). Parameter values are expressed in μm.

Trial	(d_{NN}, d_{ext})	F-ratio	p-value
Swim trial 1	(5, 50)	1.57	0.031
Swim trial 1	(5, 55)	1.632	0.028
Swim trial 1	(5, 60)	1.463	0.028
Swim trial 1	(5, 65)	1.567	0.032
Swim trial 1	(7.5, 65)	1.435	0.027
Swim trial 2	(5, 65)	1.47	0.041

Table S2: Results of the ANOVA analysis of synaptic clusters, crawl trials. To conserve space, only the 10 most significant parameter values are shown for each trial.

Trial	(d_{NN}, d_{ext})	F-ratio	p-value
Crawl trial 1	(10, 15)	1.672	0.038
Crawl trial 1	(10, 20)	1.594	0.04
Crawl trial 1	(7.5, 15)	1.958	0.038
Crawl trial 1	(7.5, 10)	1.92	0.04
Crawl trial 1	(7.5, 20)	1.831	0.038
Crawl trial 1	(7.5, 25)	1.724	0.04
Crawl trial 1	(10, 15)	1.673	0.028
Crawl trial 1	(10, 20)	1.594	0.034
Crawl trial 1	(12.5, 15)	1.533	0.028
Crawl trial 1	(12.5, 20)	1.491	0.034
Crawl trial 2	(7.5, 25)	1.786	0.028
Crawl trial 2	(7.5, 15)	1.659	0.03
Crawl trial 2	(7.5, 10)	1.640	0.029
Crawl trial 2	(7.5, 20)	1.59	0.031
Crawl trial 2	(10, 25)	1.469	0.038
Crawl trial 2	(7.5, 100)	1.423	0.035
Crawl trial 2	(12.5, 30)	1.415	0.037

Table S3: Results of the ANOVA analysis of synaptic clusters, local bend trials.

Trial	$(d_{\mathrm{NN}}, d_{\mathrm{ext}})$	F-ratio	p-value
Local bend trial 1	(5, 15)	1.37	0.048
Local bend trial 2	(5, 15)	1.726	0.036
Local bend trial 2	(5, 20)	1.756	0.03
Local bend trial 2	(5, 25)	1.751	0.03
Local bend trial 2	(5, 30)	1.735	0.031
Local bend trial 2	(5, 35)	1.735	0.021
Local bend trial 2	(5, 40)	1.735	0.021
Local bend trial 2	(7.5, 25)	1.8	0.042
Local bend trial 2	(7.5, 30)	1.722	0.042
Local bend trial 2	(7.5, 35)	1.714	0.042
Local bend trial 2	(7.5, 40)	1.805	0.038
Local bend trial 3	(5, 80)	1.52	0.039
Local bend trial 3	(5, 85)	1.525	0.039
Local bend trial 3	(5, 90)	1.525	0.037
Local bend trial 3	(5, 95)	1.525	0.04
Local bend trial 3	(5, 100)	1.526	0.037
Local bend trial 3	(7.5, 70)	1.502	0.038
Local bend trial 3	(7.5, 75)	1.591	0.034
Local bend trial 3	(7.5, 80)	1.807	0.018
Local bend trial 3	(7.5, 85)	1.768	0.022
Local bend trial 3	(7.5, 100)	1.495	0.033

Table S4: List of raw data trials and how they are referred to in the paper.

Figure	Behavior	Trial no. in paper	Trial no. in raw data
Fig. 1	Swim	1	006
–	Swim	2	008
Fig. 2	Crawl	1	015
–	Crawl	2	017
Fig. 3	Local bend	1	009
–	Local bend	2	010
–	Local bend	3	011
–	Local bend	4	012